

Surrogate-based Multidisciplinary Design Optimization of a Canard Configuration VTOL UAV

Tiago Alexandre Salreta de Jesus
tiago.d.jesus@tecnico.ulisboa.pt

Instituto Superior Técnico, Universidade de Lisboa, Portugal

January 2021

Abstract

This work presents a surrogate-based multidisciplinary design optimization (MDO) of a canard fixed-wing vertical take-off and landing (VTOL) unmanned aircraft (UAV) configuration. A detailed multi-fidelity aero-structural optimization including wing, canard, vertical surfaces as well as fuselage is carried out primarily motivated by the envisioned mission profile and stability and maneuverability requirements with the objective of maximizing range in cruise, by considering a linearization of the range variation with both the structural mass and (L/D) . The multidisciplinary analysis (MDA) includes an estimation of the aerodynamic loads based on Prandtl's lifting line theory (LLT), the calculation of the structural mass, along with the evaluation of the Tsai-Wu failure criterion for the structural elements and the determination of (L/D) from a computational fluid dynamics (CFD) analysis. Kriging based surrogate models are generated for both objective function and constraints. A combination of WB2 (Watson and Barnes criterion), Expected Improvement (EI) and prediction based search methods, along with engineering knowledge is used for surrogate models enrichment and avoid excessive exploration of the design space while aiming to achieve the global, or a local optimum that allows significant improvements. The evolution of the configurations, along with the approximation models during the iterative optimization process are illustrated using tables and plots showing performance metrics parameters, followed by an examination and discussion of the whole process evolution along with the obtained results. An analysis of the best configuration reached provides an estimation of a represented structural mass of 16.84% of the Maximum Take-Off Mass (MTOM), a stall speed of 27.61 m/s in addition to lift-to-drag ratios L/D of 16.59 in cruise and 7.90 in dash.

Keywords: Multiobjective, multi-fidelity, aero-structural, Kriging, Expected Improvement

1. Introduction

Multidisciplinary design optimization (MDO) is a field of engineering that is a very useful tool of choice in the development of aircraft designs [1]. This is due mainly to the emergence of more demanding requirements and having a higher-level aircraft design tool will provide the manufacturers leverage over the competition. MDO makes use of numerical and analytic methods to develop models integrating multiple disciplines, the most common being aerodynamics, structural behavior, weight estimation and propulsion [2]. Multiple frameworks can be implemented including either low or high fidelity (LF or HF) models to perform the multidisciplinary analysis (MDA). As the process can be very time demanding and computationally expensive, surrogate models are a viable option to mimic the behavior of the simulation models as closely as possible, being cheaper to evaluate.

This project focuses on a surrogate based mul-

tiobjective multidisciplinary design optimization of a fixed-wing, vertical take-off and landing (VTOL) canard configuration unmanned aerial vehicle (UAV) that is being developed by the University of Victoria Centre for Aerospace Research (CfAR) in collaboration with Defense Research and Development Canada (DRDC), for magnetic anomaly detection (MAD) by means of a sensor. The aircraft mission involves a vertical take-off and climb to minimum height segment, a transition to forward flight segment followed by cruise at approximately 100m above sea level and finally, a transition to axial flight and a vertical landing.

The fuselage shape and a vertical tail volume coefficient (C_{VT}) equal to 0.02 for directional stability [3], were preserved from the conceptual and preliminary design done by Bruno Luís on his master thesis [4]. The optimization is motivated by the mission requirements and involves both structural and aerodynamic variables. A description and test of

the optimal design reached follow the optimization process.

2. Background

2.1. Tsai-Wu failure criterion

Laminate composites are classified as orthotropic materials, thus having properties that are different in three mutually orthogonal directions [5]. Considering a single ply of a laminate, there are five independent strength constants that correspond to maximum allowed in-plane stresses in the principal axes. They are defined as follows:

- S_{Lt} - Longitudinal tensile strength
- S_{Lc} - Longitudinal compressive strength
- S_{Tt} - Transverse tensile strength
- S_{Tc} - Transverse compressive strength
- S_S - In-plane shear strength

Tsai and Wu suggested a quadratic criterion for a six-dimensional stress space, in which failure occurs if the following is verified:

$$F_i \sigma_i + F_{ij} \sigma_i \sigma_j = 1 \quad i, j = 1, \dots, 6, \quad (1)$$

wherein $\sigma_{1,2,3}$ are the direct stresses in each of the principal directions, the remaining stress components are $\sigma_4 = \tau_{23}$, $\sigma_5 = \tau_{31}$, $\sigma_6 = \tau_{12}$ and F_i and F_{ij} are strength tensors [6].

For a single orthotropic ply of a laminate, subject to plane stress, equation 1 is simplified to [6]:

$$F_1 \sigma_{11} + F_2 \sigma_{22} + F_6 \tau_{12} + F_{11} \sigma_{11}^2 + F_{22} \sigma_{22}^2 + F_{66} \tau_{12}^2 + 2F_{12} \sigma_{11} \sigma_{22} = 1, \quad (2)$$

where the strength coefficients can be determined by the following expressions:

$$\begin{aligned} F_1 &= \frac{1}{S_{Lt}} - \frac{1}{S_{Lc}}; & F_2 &= \frac{1}{S_{Tt}} - \frac{1}{S_{Tc}}; \\ F_{11} &= \frac{1}{S_{Lt} S_{Lc}}; & F_{22} &= \frac{1}{S_{Tt} S_{Tc}}; \\ F_6 &= 0; & F_{66} &= \frac{1}{S_S^2}. \end{aligned} \quad (3)$$

However, the in-plane interaction term F_{12} must be discovered by a bi-axial tensile test or estimated with the relation [5]:

$$-\frac{1}{2}(F_{11} F_{22})^{1/2} \leq F_{12} \leq 0. \quad (4)$$

2.2. Prandtl's Lifting Line Theory [7]

Prandtl's Lifting Line Theory (LLT) is used to demonstrate the aerodynamic behavior of straight three-dimensional wings, assuming inviscid incompressible flow. It considers wing twist as well as

varying chord and airfoil along span. However, it does not take into account dihedral or sweep on the wing.

The circulation and vortex effects of the flow shed from the wing is approximated by replacing the wing with multiple horseshoe vortices with different but constant strengths.

This allows for a distribution of circulation $\Gamma(y)$ along span, where y corresponds to a specific spanwise station, which is transformed into angular form to simplify posterior calculations:

$$y = \frac{b}{2} \cos(\theta), \quad \theta \in [0, \pi], \quad (5)$$

where b is the wingspan. The spanwise distribution of vortex strengths is represented by a Fourier sine series of N elements:

$$\Gamma(\theta) = 2bV_\infty \sum_{n=1}^N A_n \sin(n\theta), \quad (6)$$

where, V_∞ denotes the free-stream airspeed.

The trailing vortex sheet induces a downwash on the wing with velocity w_i for each spanwise section and the downwash angle is given by:

$$\alpha_i = \frac{w_i}{V_\infty}. \quad (7)$$

The local flow angle α_{2D} at each section is equal to the sum of the three-dimensional wing's angle of attack (α), plus the section twist (γ) minus the downwash angle. Knowing that the two-dimensional section lift coefficient is a function of the local flow and the bound vortex strength at this span location, it is possible to rearrange the relation expression:

$$\begin{aligned} C_{L_{2D}} &= a_0(\alpha_{2D} - \alpha_0) = \frac{2\Gamma}{V_\infty c} \\ \Leftrightarrow \Gamma &= \frac{1}{2} a_0 V_\infty c (\alpha - \alpha_i + \gamma - \alpha_0), \end{aligned} \quad (8)$$

where, a_0 , c and α_0 are the lift slope, the chord and the zero lift angle for the considered section, respectively.

Equations 6 and 8 can be combined to form the monoplane equation. Considering the simplification $\mu = \frac{a_0 c}{4b}$, the latest is given by:

$$\begin{aligned} \sum_{n=1}^N (A_n \sin(n\theta) (\sin\theta + n\mu)) &= \\ &= \mu(\alpha + \gamma - \alpha_0) \sin\theta. \end{aligned} \quad (9)$$

In order to solve for the coefficients A_n , the previous equation is applied for all N spanwise stations. Subsequently, the lift, and accordingly the lift induced drag, are obtained from the following expressions, respectively.:

$$L = \rho V_\infty \int_{-\frac{b}{2}}^{\frac{b}{2}} \Gamma(y) dy, \quad (10)$$

$$D_i = -\rho \int_{-\frac{b}{2}}^{\frac{b}{2}} w_i(y) \Gamma(y) dy \quad (11)$$

$$\Rightarrow D_i = \frac{\rho V_\infty^2}{2} b^2 \pi \sum n A_n^2 .$$

2.3. Weighted sum method [1]

The Weighted sum method makes use of a vector of weights \mathbf{w} to define priorities between objectives of an optimization. The weight vector transforms the multiobjective functions \mathbf{f} into a combined single objective f :

$$f(\mathbf{x}) = \mathbf{w}^\top \mathbf{f}(\mathbf{x}) , \quad (12)$$

where, \mathbf{x} are the design points and the elements of \mathbf{w} are non-negative, sum to one when non-dimensionalized, and each one is associated with a different objective.

2.4. Latin-Hypercube Sampling

Latin-Hypercube sampling is an uniform projection plan, that is, it has an uniform distribution of points over each dimension, meaning that projections on the axis of each dimension do not overlap [8].

A Latin-Hypercube is built by gridding the design space and splitting it in equal sized boxes. It is a generalization of a Latin square to any number of dimensions. A Latin square is a $n \times n$ grid filled with n different numbers, where each row and each column has exactly one of each numbers. For a $n \times n$ grid, the distribution of n points can be done with a permutation of n elements. Therefore, Latin-Hypercube samples can be obtained using a permutation in each dimension.

2.5. Kriging Model [8]

The Kriging model is used to estimate the response of a function at an unsampled location. Assuming that the deterministic value of $y(\mathbf{x})$ results from a stochastic process $Y(\mathbf{x})$, it can be represented by:

$$Y(\mathbf{x}) = \mu_m + \epsilon(\mathbf{x}) , \quad (13)$$

where μ_m is the mean of the response at a sampled design point and $\epsilon(\mathbf{x})$ is the error that represents the fluctuations around the trend obtained from a stationary Gauss process.

The adequate parameters to build the model are determined by the maximum likelihood estimation (MLE) method. The estimates for μ_m and the variance of the Gauss distribution σ^2 are given by:

$$\hat{\mu}_m = \frac{\mathbf{1}^\top \Psi^{-1} \mathbf{y}}{\mathbf{1}^\top \Psi^{-1} \mathbf{1}} , \quad (14)$$

$$\hat{\sigma}^2 = \frac{(\mathbf{y} - \mathbf{1}\hat{\mu}_m)^\top \Psi^{-1} (\mathbf{y} - \mathbf{1}\hat{\mu}_m)}{n} , \quad (15)$$

where, $\mathbf{y} = [y^{(1)}, \dots, y^{(n)}]$ are the function evaluations of the sample points, n is the number of

samples and Ψ is the correlation matrix for the observed data, with the correlation between to points being given by the squared exponential kernel function.

Additionally, the MLE is used to calculate the prediction of the true function and an estimate of the variance of the prediction, given by equations 16 and 17, respectively:

$$\hat{y}(\mathbf{x}) = \hat{\mu}_m + \boldsymbol{\psi}^\top \Psi^{-1} (\mathbf{y} - \mathbf{1}\hat{\mu}_m) , \quad (16)$$

$$\hat{s}^2(\mathbf{x}) = \sigma^2 \left[1 - \boldsymbol{\psi}^\top \Psi^{-1} \boldsymbol{\psi} + \frac{1 - \mathbf{1}^\top \Psi^{-1} \boldsymbol{\psi}}{\mathbf{1}^\top \Psi^{-1} \mathbf{1}} \right] , \quad (17)$$

where $\boldsymbol{\psi}$ is the vector of correlations between the observed data and the new prediction.

2.6. Expected Improvement

The Expected Improvement (EI) exploration is a more global search criterion that focuses the exploration on maximizing the expected improvement over the current best function evaluation, y_{min} .

Improvement for a function sampled at \mathbf{x} producing $y = f(\mathbf{x})$ is defined as [1]:

$$I(y) = \begin{cases} y_{min} - y, & \text{if } y < y_{min} \\ 0, & \text{otherwise} \end{cases} . \quad (18)$$

Correspondingly, the probability of such improvement can be calculated [8]:

$$P[I(\mathbf{x})] = \frac{1}{\hat{s}\sqrt{2\pi}} \int_{-\infty}^0 e^{-[I-\hat{y}(\mathbf{x})]^2/(2s^2)} dI , \quad (19)$$

where, s^2 is the Kriging model variance estimate. At already sampled points, where the measurements are noiseless, the probability of improvement, $P[I(\mathbf{x})]$ and thus the expected improvement, $E[I(\mathbf{x})]$, will both be null as the objective values at those points are already known. Having this, and knowing \hat{y} and \hat{s}^2 , the expected improvement using a distribution predicted by a Gaussian process is given by [8]:

$$E[I(y)] = \begin{cases} (y_{min} - \hat{y}(\mathbf{x})) \Phi \left(\frac{y_{min} - \hat{y}(\mathbf{x})}{\hat{s}(\mathbf{x})} \right) \\ + s\phi \left(\frac{y_{min} - \hat{y}(\mathbf{x})}{\hat{s}(\mathbf{x})} \right) \end{cases} , \quad \text{if } s > 0 ,$$

$$= \begin{cases} 0, & \text{if } s = 0 \end{cases} , \quad (20)$$

where, $\Phi(\cdot)$ is the cumulative distribution function and $\phi(\cdot)$ probability density function.

2.7. WB2 and WB2S

On the other hand, the Watson and Barnes criterion (WB2) provides a balance between exploration and exploitation. It is more local than the EI criterion as it consists on a similar expression with an additional term corresponding to the predicted value [9]:

$$WB2 = \begin{cases} \hat{y}(\mathbf{x}) + E[I(y)], & \text{if } s > 0 \\ 0, & \text{if } s = 0 \end{cases}. \quad (21)$$

Further, there is the WB2S method [10], that only differs from WB2 by adding a non-negative scaling factor s_f to the expected improvement:

$$WB2S = \begin{cases} \hat{y}(\mathbf{x}) + s_f E[I(y)], & \text{if } s > 0 \\ 0, & \text{if } s = 0 \end{cases}. \quad (22)$$

The scaling factor is added to keep the exploration property of the expected improvement, since in WB2 the magnitude of the term $E[I(y)]$ is expected to decrease during the iterative process, possibly leading the optimization to a local minimum [10].

2.8. Probability of feasibility

A possible approach for constrained problems is to merge the existing constraints with the objective function all together in a new search function that will run unconstrained.

Similarly to the calculation of the probability of improvement shown in equation 19, by following the same logic, and if the constraints are also modeled by surrogates, the probability of the prediction being greater than the constraint limit, i.e., the probability that the constraint is met $P[F(\mathbf{x})]$, or probability of feasibility (PF) is obtained by:

$$P[F(\mathbf{x})] = \frac{1}{\hat{s}\sqrt{2\pi}} \int_0^\infty e^{-[F-\hat{g}(\mathbf{x})]^2/(2\hat{s}^2)} dG, \quad (23)$$

where, g is the constraint function, g_{min} is the minimum allowed value, $F = G(\mathbf{x}) - g_{min}$ is the measure of feasibility, $G(\mathbf{x})$ is a random variable and \hat{s}^2 corresponds to the variance of the model of the constraint [8].

Assuming that the objective function and the constraints are uncorrelated, and thus both models are independent, $P[F(\mathbf{x})]$ can be coupled to the probability of improvement [8]:

$$P[I(\mathbf{x}) \cap F(\mathbf{x})] = P[I(\mathbf{x})]P[F(\mathbf{x})]. \quad (24)$$

Likewise, $P[F(\mathbf{x})]$ can be combined with multiple search functions, such as EI, WB2 and WB2S, for example.

3. Implementation

3.1. Problem Formulation

In addition to the mission profile, a list of demands provided by DRDC allowed to identify the requirements, including a specified Maximum Take Off Mass (MTOM), a minimum (dash) speed to allow progression in extreme wind conditions, minimum static stability and maneuverability requirements (table 1).

Table 1: Aircraft requirements for forward flight. *The static margin is given in percentage of the mean aerodynamic chord (MAC).

MTOM	25 kg
Cruise speed	35 m/s
Dash speed	60 m/s
Stall speed	20 m/s
Maximum operational Load factor	3g
Static margin (K_n)	10% MAC*
C_{VT}	0.02

One major drawback of the configuration is the requirement that the canard stalls before the wing for stability reasons, preventing the aircraft wing to achieve near stall C_L values.

Taking into account the given requirements, the ultimate objective of the optimization problem is to maximize range in cruise.

As there is not enough information about the propulsion system to be used on the UAV, a multiobjective optimization including (L/D) and the structural mass m_S is chosen. The weighted sum method allows to merge both objectives into a single function that measures the variation of range relative to a reference aircraft configuration. The objective function is then given by:

$$\frac{\Delta R}{R_{ref}} = \frac{\Delta(L/D)}{(L/D)_{ref}} - \frac{\ln\left(1 + \frac{m_{S_{ref}}}{m_{f_{ref}}}\right)}{\ln\left(\frac{m_i}{m_{f_{ref}}}\right)} \frac{\Delta m_S}{m_{S_{ref}}}, \quad (25)$$

where, (L/D) , m_i and m_f are the lift to drag ratio, the initial mass and the final mass at the end of the mission segment, respectively, and also, $\Delta(L/D) = (L/D) - (L/D)_{ref}$ and $\Delta m_S = m_S - m_{S_{ref}}$.

Therefore, the weights of each component of the objective are defined as 1 and $-\ln\left(1 + \frac{m_{S_{ref}}}{m_{f_{ref}}}\right) / \ln\left(\frac{m_i}{m_{f_{ref}}}\right)$ for (L/D) and m_S , respectively.

For the first reference configuration it was assumed that the structural mass was 50% of the empty aircraft mass (m_f). This assumption was somewhat arbitrary but considered reasonable by the author.

The structural mass fraction of the empty mass is updated whenever the reference configuration,

which will always correspond to the best configuration from the current set of analyzed configurations. A configuration is considered the best if it is feasible and has the highest value of the prevailing objective function from all the samples. The new final and structural reference masses will correspond to the previous plus the variation of structural mass from the prior best configuration.

In order to evaluate the (L/D) and m_S values, aerodynamic and structural models were built from a parameterization based on a total of 37 design variables, defining the wing, winglet, canard, fin and fuselage.

The wing is defined using variables corresponding to span, leading edge sweep angle and bilinear chord and twist distributions (four variables for each distribution). Identically, the wingbox skin and spars thickness distributions are also bilinear. A trapezoidal winglet geometry parameterization is also included, specified by span, taper ratio and winglet sweep.

The canard planform is rectangular with variable area, span, as well as vertical and longitudinal positions. A constant thickness tube is the structure modeled to support the canard loads. The radius and thickness of the tube are also design variables.

Root chord, taper ratio and span are the parameters defining the vertical fin.

All airfoils are defined by the NACA 4-digit airfoil parameterization [11].

Lastly, the structure of the fuselage consists on two identical laminate spars with constant thickness, parallel to each other along the length of the fuselage. As regards the baseline shape of the fuselage, it was previously defined by Bruno Luís in his master thesis [4]. Spanwise and transverse fuselage scaling factors are applied to obtain the final shape and size of the fuselage, and together with the spar thickness, form the set of design variables for the fuselage.

Aiming to reduce the computational resources required for the optimization, namely HF CFD analyses, constraints related to geometry, trim conditions, longitudinal, directional and lateral stability and stall conditions were taken as considerations either in the definition of the design variables and their boundaries, by imposing dimensional relations, or during the analysis of the different configurations, by allowing the position of the center of gravity (CoG), the incidence of the canard i_c and the angle of attack (AoA) α to change in each analysis. Since the modeled structure is assumed to be entirely made of Carbon Fiber Reinforced Polymers (CFRP), the only constraint included in the optimization procedure is the Tsai-Wu failure criterion for composite materials at the ultimate load case considered, with a vertical load factor of 4.5g.

The feasible region regarding this constraint will be where the Tsai-Wu failure index is smaller than 1.

3.2. MDA Procedure

The analysis conducted throughout this project can be divided in four major steps:

1. Generation of two geometries to be used in the structural and aerodynamic analysis, respectively, based on the inputs for the design variables.
2. An initial LF estimation of the aerodynamic loading based on Prandtl's LLT for a trimmed aircraft, considering the ultimate load case of 4.5g.
3. A structural finite elements method (FEM) analysis executed in ANSYS Mechanical APDL to calculate m_S as well as to evaluate the structural integrity of the UAV by applying the previously determined aerodynamic loads and the Tsai-Wu failure criterion to all elements.
4. A HF CFD analysis performed in ANSYS CFX is used to determine the position of the CoG, α , i_c and (L/D) for the established trim and stability conditions, by assuming that both the lift and pitching moment coefficients (C_L and C_m) vary linearly with α and i_c and then solving the following system of equations:

$$\begin{cases} C_{L_{trim}} = \frac{dC_L}{d\alpha} \alpha_{trim} + \frac{dC_L}{di_c} \Delta i_c \\ \quad + C_{L_{\alpha=0}} \\ C_{m_{trim}} = \frac{dC_m}{d\alpha} \alpha_{trim} + \frac{dC_m}{di_c} \Delta i_c \\ \quad + C_{m_{\alpha=0}} \end{cases}, \quad (26)$$

where, Δi_c , $C_{L_{\alpha=0}}$ and $C_{m_{\alpha=0}}$ are the difference between $i_{c_{trim}}$ and a first rough estimation of i_c , and the values of C_L and C_m for an AoA of zero degrees, respectively, and $C_{m_{trim}} = 0$.

The analysis of each configuration is sequential, following the presented order. Moreover, step 4 is only performed if the configuration proves to be structurally feasible on the previous step. The whole process is represented on the following flowchart (figure 1).

3.3. MDO methodology

Three Kriging based surrogate models were built with the DACE MATLAB toolbox [12] for a complete approximation of the solution. Two of them were generated from the structural data, modeling the constraint value (Tsai-Wu failure index), and the structural mass required for the objective function, respectively. These include all design variables and represent 37-dimensional spaces. The other model represents the performance ratio

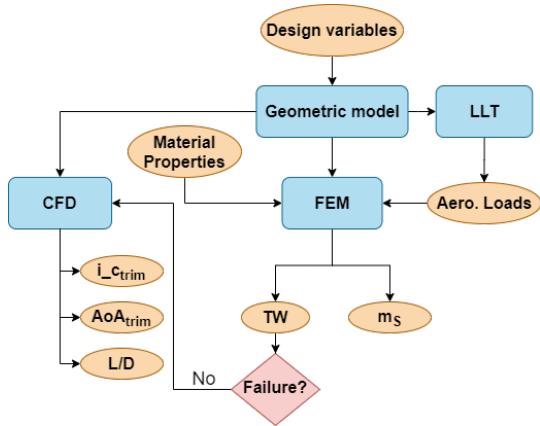


Figure 1: MDA architecture.

(L/D) , resultant from the aerodynamic data. Differently, the (L/D) model only includes 27 dimensions, as there are 10 exclusively structural variables. A sampling plan with 41 samples, obtained from Latin-Hypercube sampling, was employed to generate the initial surrogates. All three models were initially implemented with a constant regression, as it showed to be the most accurate for the two structural models and it was the only option for the (L/D) model since only 8 of the initial samples were structurally feasible, and thus available to build the (L/D) surrogate. In all three models, the fluctuations around the trend are determined by Gauss correlations, also included in the used toolbox.

Eight search methods are considered for the defined optimization problem, being these the EI, WB2, WB2S, prediction-based exploration (\hat{y}), and all the previous with the implementation of the PF. All methods are used at each iteration to define eight different search functions.

The search is then performed by a GA. The MATLAB ‘ga’ function is used for this purpose.

All methods will generate one new potential sample point per iteration. The new point is then chosen by the author after an analysis based on a set of criteria and on experience. The points originated from WB2 and WB2S have priority. The one with the best predictions for the objective function and/or higher uncertainty in the first iterations is selected. If both turn out to be structurally unfeasible, the previous criteria should be applied to the remaining methods. If none of the points is appropriate for evaluation or feasible, the points that had the structural mass and Tsai-Wu failure index calculated are added to update the two structural models and the optimization is reiterated. Each complete optimization iteration cycle is performed according with the scheme displayed in figure 2. The cycle is repeated until either the outputs from

the GA converge to an optimum or there is no more time available for further iterations.

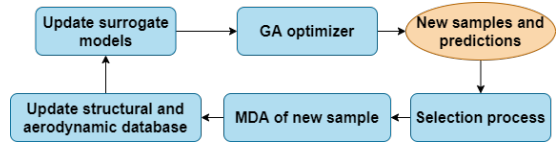


Figure 2: Optimization iteration cycle.

4. Post-Processing

4.1. Discussion of Results

The optimization was initiated with the initial sample number 5 set as reference, with the corresponding reference values: $m_{S_{ref}} = 9.731kg$; $m_{f_{ref}} = 19.462kg$; $(L/D)_{ref} = 13.6$.

As the aerodynamic analysis is much more time-consuming than the structural analysis, multiple points were selected per iteration to calculate m_S and the Tsai-Wu failure index, while only one of them would go through the CFD analysis, which runs in parallel with the structural analysis of the remaining points. This strategy aims to improve the approximation of the structural boundary for a more precise exploration within the feasible region. At the end of the optimization a total of 276 samples were structurally analyzed, of which only 14.5% were fully evaluated. Also, the computational resources available made it possible to run two CFD analyses at the same time in some occasions. When this was true, a design would be created by the author, based on the current best configurations with additional modifications towards a design with higher (L/D) . The two configurations were analyzed in parallel. These manually introduced samples correspond to 4% of the total 276.

With the increase of the number of samples, the m_S surrogate showed better approximations when build with a linear regression, while the constraint and the (L/D) models were better approximated by a constant regression. The mass model was the most accurate of the two structural models with an average error of 5% in comparison with 40% verified for the constraint, indicating that the failure criterion is represented by a more complex function. In contrast, the (L/D) model displayed an average error of 7%, almost identical to m_S , as its construction is based on only 27 variables against the 37 used for the structural models, even with significantly less samples for the model construction.

Figures 3, 4, 5, plot the evolution along the optimization of m_S , (L/D) and the Tsai-Wu failure index, respectively. Only samples corresponding to iterations with complete aero-structural evaluations are displayed. The initial samples are represented in black on the negative side of the horizontal axis, green points correspond to samples generated by

the optimization and blue points to the configurations introduced by the author.

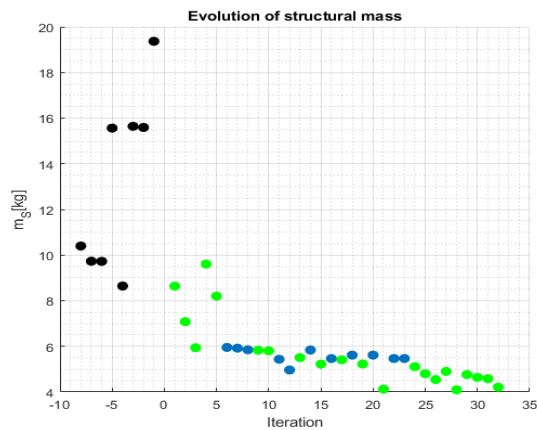


Figure 3: Evolution of m_S along the optimization.

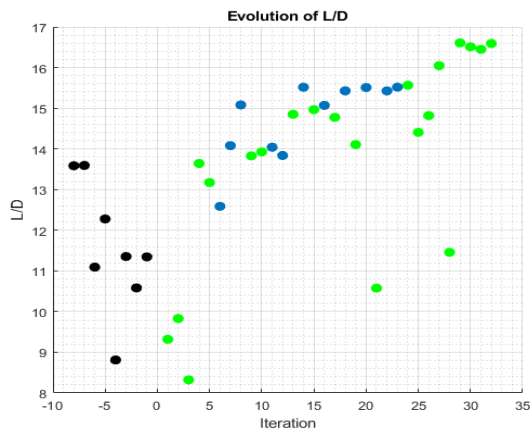


Figure 4: Evolution of (L/D) along the optimization.

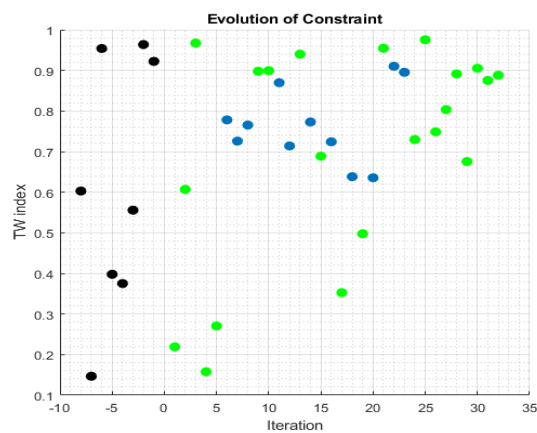


Figure 5: Evolution of the Tsai-Wu failure index along the optimization.

Due to a low percentage of feasibility of the selected design points along the optimization due to the high uncertainty on the constraint model, it was decided to sweep the seven structural design variables of the wing, in order to identify their influence on the structural models, and to improve the prediction of the Tsai-Wu boundary. A total of 79 configurations were generated and structurally analyzed, allowing to reduce the uncertainty of the constraint model by 34%.

Figures 6 and 7 plot the evolution along the optimization of the objective function ΔR and the ratio R/R_{ref_0} , respectively, where R_{ref_0} is the range of the initial reference configuration. The color scheme used to represent the design points at each iteration corresponds to the one applied in figures 3, 4 and 5.

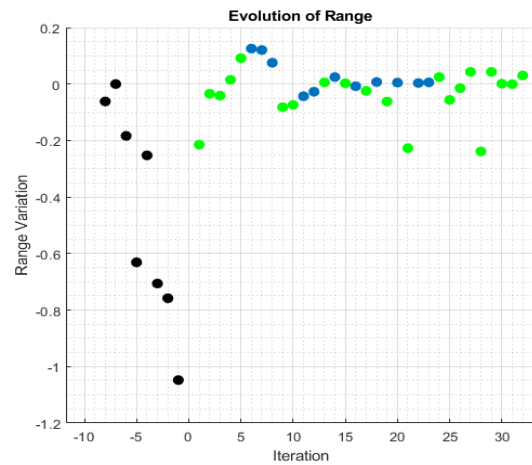


Figure 6: Evolution of the objective function along the optimization.

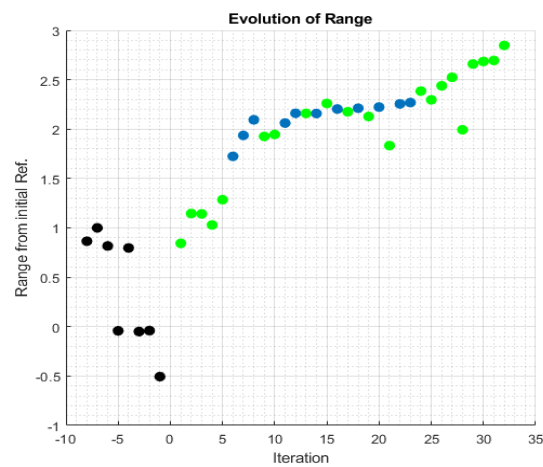


Figure 7: Evolution of range ratio, R/R_{ref_0} along the optimization.

It is verified that range is increasing along the optimization and starts converging with ΔR tending to zero with the number of iterations. Similarly to the (L/D) , the author's predictions represent most of the greater improvements in range, as (L/D) has a higher influence on range than m_S . This is due to the fact of the weight of the mass component in the objective function, $-\ln\left(1 + \frac{m_{S_{ref}}}{m_{f_{ref}}}\right) / \ln\left(\frac{m_i}{m_{f_{ref}}}\right)$, decreasing its magnitude with the reduction of m_S , having an initial magnitude of 0.8911, smaller than the weight of the (L/D) component in the objective function, which is constant and equal to 1.

The optimal configuration developed in such way to increase the aspect ratio of both wing and canard, in particular, the average aspect ratios of the first 10 iterations are 11.28 and 15.35, while for the last 10 iterations are 13.33 and 18.98, for the two lifting surfaces, respectively. It is also verified that the AoA is gradually smaller in magnitude, as the optimization adapts the incidence and twist angles of the wing and, along with i_c , tries to trim the aircraft aligned with the flow, thus reducing the fuselage drag. Consequently, (L/D) and range increase.

Structurally, the component which had the highest Tsai-Wu failure index in almost all iterations was the fuselage spar in the region of the connection with the canard tube. A possible approach to improve this feature could be to strengthen the fuselage spar laminate in the region around the canard, allowing the rest of the spar to be thinner, thus significantly decreasing the structural mass.

The optimization was stopped after iteration 32 because the time limit was reached. Nevertheless, it can be considered approximately converged as in the last 5 iterations that had an improvement in range, the relative variation of range is always smaller than 5%. However, the last iteration showed an improvement of 3%, whereas the previous improvement was only of 0.1%, meaning that the result could be further optimized.

It cannot be verified if the exploited optimum region corresponds to a local or a global optimum. Moreover, the existence of designs with negative objective values in the latter iterations, indicate that the optimizer is not being able to find better predictions than the ones already existing, meaning that the current optimum is located in a valley of the design space.

Figure 8 displays the Pareto frontier of the problem, with the horizontal and vertical axes corresponding to m_S and (L/D) , respectively. It shows that 21 points, which correspond to 66% of the new fully-evaluated samples, are inside a good feasible region with the structural mass between 4 and 6 kilograms, and (L/D) between 14 and 17.

Additionally, the optimization seems to be devel-

oping towards a utopia point, in the top left corner of figure 8, with $m_S = 4kg$ and $(L/D) = 17$, although this point might not be possible to reach.

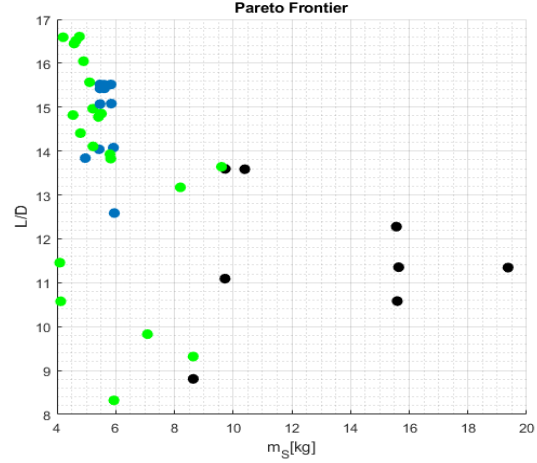


Figure 8: Pareto frontier.

4.2. Characterization and validation of final design

The achieved optimum design point has the following outputs: $m_S = 4.209kg$; $m_f = 13.940kg$; $(L/D) = 16.6$; $R/R_{ref_0} = 2.847$. It represents a reduction of 56.7% in the structural mass, which corresponds to 16.84% of the MTOM, along with an increase of 22.1% in (L/D) , from the initial reference sample, resulting in a range almost three times larger than R_{ref_0} in cruise. The region of the fuselage spar around the connection with the canard displayed the maximum Tsai-Wu failure index, with a value of 0.89. The trim and stability conditions in cruise were verified for a combination of $\alpha_{trim} = 1.6^\circ$, $i_{c_{trim}} = 1.3^\circ$ and a distance between the CoG and the wing aerodynamic center $l_w = 0.338m$. Additionally, the final design exhibits a value of 7.9 for (L/D) in dash. The resulting structure and outer shape are represented on figures 9 and 10, respectively.

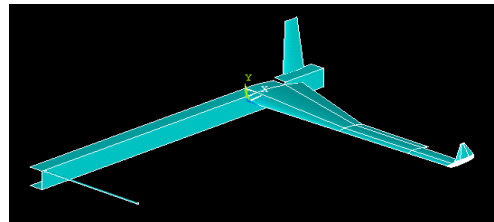


Figure 9: Representation of the structure of the final configuration.

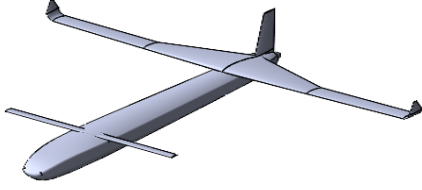


Figure 10: Representation of the outer shape of the final configuration.

Figure 11 depicts the three main dimensions of the aircraft with $a = 2.653m$, $b = 0.540m$ and $c = 2.838m$.

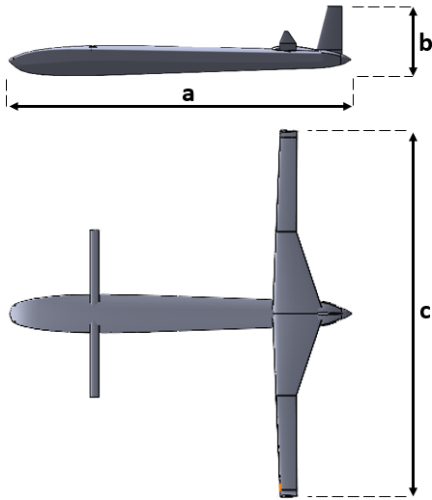


Figure 11: Aircraft dimensions.

A thorough analysis of the final design allows a more complete characterization. The fuselage is short and slender, thus with a reduced surface area in order to decrease drag. The fin is big, almost set to the upper bounds of the design variables, allowing it to be placed closer to the CoG, in particular, at the trailing edge of the wing, while still complying with the stability requirements. This contributes to the reduction of the fuselage length. Differently, the canard is relatively small, located at the top of the fuselage. Its position is such that its trailing stream interferes with the wing by increasing drag and unloading the wing closer to the root. Further, the two lifting surfaces show high drag, with the wing being responsible for approximately 50% of the total drag and the canard displaying practically the same contribution as the fuselage to the drag of the aircraft. It was also verified that the canard stalls for an AoA of 12 degrees and $C_{L_{c_{max}}} = 1.327$, while the wing stalls at $\alpha = 13.5^\circ$ for $C_{L_{w_{max}}} = 1.204$, thus confirming the requirement which imposes that the canard must stall before the wing. This translated in an estimated stall

speed of $27.61m/s$, which is 38% higher than the desired $20m/s$. This value was obtained by trimming the aircraft with $C_{L_c} = C_{L_{c_{max}}}$.

Regarding the structure of the aircraft, the fuselage spar thickness converged to its minimum allowed value, indicating that it could possibly be reduced while maintaining integrity. The canard tube has a total of 30 composite layers, in comparison with the imposed minimum of 6. An alternative structure for the canard, for example, include a carbon fiber skin capable of bearing part of the loads, should be considered to reduce the tube thickness. Also, the wingbox thickness distribution displays a smaller thickness at the root for both skin and spars, with the maximum thickness being located at the spanwise position of discontinuity of the wing. This thickness distribution is possibly due to the fact of the wing section being larger closer to the root, which translates in a higher inertia and thus a smaller required thickness. The opposite happens from the discontinuity to the tip.

Additionally, a modal analysis performed on the structure allowed to identify the first ten mode shapes and respective frequencies presented on table 2. The axes X , Y and Z , indicated in table 2, correspond to the directions of the roll, pitch and yaw axes of the aircraft, respectively.

Table 2: Mode shapes and respective frequencies.

Frequency [Hz]	Mode	Location
12.863	Bending Z	Wing
21.389	Bending $Z + X$	Canard
21.470	Bending $X + Z$	Canard
22.958	Bending $Z + X$	Canard
27.387	Bending X	Fin
43.023	Bending Z	Wing
61.991	Bending X	Wing
75.561	Bending Z	Fuselage
91.112	Torsion Y	Wing
109.74	1) Torsion Y 2) Bending X	1) Wing 2) Fin

5. Conclusions

The gathered results show that the optimization was successful, as significant improvements in range were achieved, with the optimum found exhibiting a range almost the triple of the initial reference. Nevertheless, the MDO would benefit of additional time to run more iterations, as the last iteration showed an increase in the variation of range, indicating that further improvements could still be achieved before reaching convergence.

Also, the detailed characterization and validation of the the final configuration demonstrated that the constraints and requirements were met, except the one for the stall speed. The final design also re-

vealed some drawbacks related to drag and interference between the wing and canard air flows. Modifications on the canard design should be considered targeting a better overall performance. In particular, increasing its area would allow to trim the aircraft for higher values of lift coefficient on the wing, consequently reducing the stall speed. Furthermore, lowering its position would reduce the interference on the airflow around the wing, allowing a more intense loading of the wing closer to the root, which would make the wing lift distribution more elliptical, thus reducing drag.

Other limitation was the lack of automation between the different stages of each iteration, such as the transfer of data from one software to another, as well as the update of the database and the surrogate models, making it necessary for the author to perform these tasks manually, which was very time consuming. A more continuous analysis would allow the optimization to run autonomously for longer periods, reducing the number of manual interventions required.

Further, the learning and prediction process of the Kriging surrogate models showed a slow development in this problem and it is mostly data driven, requiring a large quantity of sampled input information to make satisfactory predictions and explore desired regions of the design space. A possible approach could be to remove some of the black-box limitations of surrogate modeling by adding features to the search methods that give preference to certain regions of the design space based on empirical knowledge. For example, promoting configurations with higher aspect ratios or configurations that can be trimmed at a small AoA, being aligned with the flow in an ideal condition, as these two factors are known to contribute to the increase of (L/D) . It could be implemented in a similar way to the PF, except instead of prioritizing designs that are more likely to be feasible, it would give more weight to designs that are expected to possess the desired properties.

Finally, the next task should be proceed to the detailed design of the UAV. It is important to identify all the components to integrate in the aircraft, as well as position them taking into account the desired CoG position. Additionally, the propulsive design should be of special focus, as a fully defined propulsion system will allow the absolute quantification of range, instead of the relative improvements obtained so far.

References

- [1] Mykel J. Kochenderfer and Tim A. Wheeler. *Algorithms for Optimization*. MIT Press, 1st edition, 2019.
- [2] Athanasios Papageorgiou, Mehdi Tarkian,

Kristian Amadori, and Johan Ölvander. Multidisciplinary design optimization of aerial vehicles: A review of recent advancements. *International Journal of Aerospace Engineering*, 2018, 2018.

- [3] T. C. Corke. *Design of Aircraft*. Pearson Education, 2002.
- [4] Bruno Miguel Wong Luís. Design and development of a magnetic anomaly detection unmanned aerial vehicle. Master's thesis, Instituto Superior Técnico, 2019.
- [5] F.C. Campbell. *Structural Composite Materials*, chapter 16. ASM International, 2010.
- [6] Robert M. Jones. *Mechanics of composite materials*, chapter 2. Taylor & Francis, Inc., 1999.
- [7] Snorri Gudmundsson. *General Aviation Aircraft Design: Applied Methods and Procedures*, chapter 9, pages 379–389. Butterworth-Heinemann, 2014.
- [8] András Sóbester Alexander I.J. Forrester and Andy J. Keane. *Engineering design via surrogate modelling : a practical guide*. John Wiley & Sons Ltd., 1st edition, 2008.
- [9] Panos Papalambros, Pierre Goovaerts, and Michael J Sasena. Exploration of Meta-modeling Sampling Criteria for Constrained Global Optimization. *Engineering Optimization*, 34(3):263–278, 2002.
- [10] N. Bartoli, T. Lefebvre, S. Dubreuil, R. Olivanti, R. Priem, N. Bons, J. R.R.A. Martins, and J. Morlier. Adaptive modeling strategy for constrained global optimization with application to aerodynamic wing design. *Aerospace Science and Technology*, 90:85–102, 2019.
- [11] Kenneth E. Ward Eastman N. Jacobs and Robert M. Pinkerton. The characteristics of 78 related airfoil sections from tests in the variable-density wind tunnel. Report 460, National Advisory Committee for Aeronautics, 1933.
- [12] Hans Bruun Nielsen Søren N. Lophaven and Jacob Søndergaard. Dace - a matlab kriging toolbox. Technical Report IMM-TR-2002-12, Technical University of Denmark, August 2002. Version 2.0.